

RESEARCH

Open Access



# Depletion of LONP2 unmasks differential requirements for peroxisomal function between cell types and in cholesterol metabolism

Akihiro Yamashita<sup>1,2</sup>, Olesia Ignatenko<sup>1</sup>, Mai Nguyen<sup>1</sup>, Raphaëlle Lambert<sup>3</sup>, Kathleen Watt<sup>4</sup>, Caroline Daneault<sup>5</sup>, Isabelle Robillard-Frayne<sup>5</sup>, Ivan Topisirovic<sup>6,7,8,9</sup>, Christine Des Rosiers<sup>5</sup> and Heidi M. McBride<sup>1\*</sup>

## Abstract

Peroxisomes play a central role in tuning metabolic and signaling programs in a tissue- and cell-type-specific manner. However, the mechanisms by which the status of peroxisomes is communicated and integrated into cellular signaling pathways are not yet understood. Herein, we report the cellular responses to peroxisomal proteotoxic stress upon silencing the peroxisomal protease/chaperone LONP2. Depletion of LONP2 triggered the accumulation of its substrate TYSND1 protease, while the overall expression of peroxisomal proteins, as well as TYSND1-dependent ACOX1 processing appeared normal, reflecting early stages of peroxisomal proteotoxic stress. Consequently, the alteration of peroxisome size and numbers, and luminal protein import failure was coupled with induction of cell-specific cellular stress responses. Specific to COS-7 cells was a strong activation of the integrated stress response (ISR) and upregulation of ribosomal biogenesis gene expression levels. Common changes between COS-7 and U2OS cell lines included repression of the retinoic acid signaling pathway and upregulation of sphingolipids. Cholesterol accumulated in the endomembrane compartments in both cell lines, consistent with evidence that peroxisomes are required for cholesterol flux out of late endosomes. These unexpected consequences of peroxisomal stress provide an important insight into our understanding of the tissue-specific responses seen in peroxisomal disorders.

## Introduction

Peroxisomes are ubiquitous eukaryotic organelles that are central to the regulation of lipid metabolism, redox regulation and signaling [52]. The precise function of peroxisomes is coupled to cellular demand and the metabolic wiring within a given tissue [13]. Peroxisomal metabolic pathways include catalase-mediated reduction of peroxide to water and beta-oxidation of very long chain or branched chain fatty acids. Once fatty acid chains are

reduced to shorter lengths, they are transferred to mitochondria for completion of beta-oxidation [52]. In liver, peroxisomes function with mitochondria and the endoplasmic reticulum (ER) to generate bile acids, a process that can utilize up to 90% of newly synthesized cholesterol in rodents [49]. In the brain, peroxisomal factors are enriched in astrocytes compared to neurons, and cultured astrocytes but not neurons demonstrate beta-oxidation activity [8, 18, 26, 40]. In oligodendrocytes, a primary function of peroxisomes is the generation of plasmalogen ether lipids, as these lipids synthesized in peroxisomes and ER are essential for myelin formation by these cells [21]. These examples highlight the fact that the mass metabolic flux through peroxisomes varies greatly

\*Correspondence:

Heidi M. McBride

heidi.mcbride@mcgill.ca

Full list of author information is available at the end of the article



© The Author(s) 2023. **Open Access** This article is licensed under a Creative Commons Attribution 4.0 International License, which permits use, sharing, adaptation, distribution and reproduction in any medium or format, as long as you give appropriate credit to the original author(s) and the source, provide a link to the Creative Commons licence, and indicate if changes were made. The images or other third party material in this article are included in the article's Creative Commons licence, unless indicated otherwise in a credit line to the material. If material is not included in the article's Creative Commons licence and your intended use is not permitted by statutory regulation or exceeds the permitted use, you will need to obtain permission directly from the copyright holder. To view a copy of this licence, visit <http://creativecommons.org/licenses/by/4.0/>. The Creative Commons Public Domain Dedication waiver (<http://creativecommons.org/publicdomain/zero/1.0/>) applies to the data made available in this article, unless otherwise stated in a credit line to the data.

depending on the tissue and need. Pathologies arise when peroxisomal function is altered by pathogenic variants. Peroxisomal biogenesis diseases are the most severe, manifesting with multisystemic developmental pathologies, growth failure, and early lethality [52]. Peroxisomal dysfunction is also associated with ageing, cancer, and neurodegenerative diseases, likely contributing to the pathogenesis of common diseases [50, 55].

A key open question is how peroxisomes may communicate their status through stress responses and retrograde signaling pathways. New approaches to monitor transcriptional, lipidomic and proteomic changes in conditions of induced peroxisomal stress, primarily through the targeted loss of proteins essential for peroxisomal import, shed light on generalized organellar dysfunction. While global cellular stress responses are elicited in these conditions, there is a surprising variability in the details of these responses depending on the specific import component under investigation, the cell or tissue type and the model organism used [25, 37, 53]. This hints that peroxisomal stress may not always lead to comparable stress responses, likely reflecting distinct functions of peroxisomal import components and their clients.

The loss of peroxisome import provides an excellent experimental approach to reduce or block peroxisomal function. In this study, we took a different approach to specifically monitor the stress response driven by an accumulation of unfolded proteins within the peroxisomal lumen. Currently, Lon peptidase 2 (LONP2) is the only known peroxisomal protease that is conserved in plants, fungi and mammals [12]. LONP2 is the product of an early gene duplication of mitochondrial LONP1, which was retained from its bacterial origin [11]. Lon peptidases act as both a chaperone and an ATP dependent protease responsible for the degradation and turnover of oxidized proteins in bacteria, mitochondria, peroxisomes and chloroplasts [47, 54]. Studies have directly investigated the biochemistry and substrates of peroxisomal LONP2, where the protease TYSND1, which is responsible for the processing of peroxisomal enzymes including ACOX1 (Kurochkin et al., 2007), is one substrate identified in mammalian cells [31], and other clients including catalase have been identified in the fungi *P. chrysogenum* and *H. polymorpha* [1, 2]. In addition to LONP2 protease activity, its chaperone function was illustrated by the development of significant peroxisomal protein aggregates upon loss of LONP2 in fungi, thereby demonstrating that loss of LONP2 induced proteotoxic stress [1, 2]. While the function of LONP2 as a key regulator of peroxisomal protein turnover and homeostasis is widely accepted, the functional consequences of these processes have not been explored in mammalian cells [36]. To map the peroxisomal proteotoxic stress response

that could be independent from a total loss of protein import, we took an siRNA approach to acutely silence expression of LONP2 in two distinct cell lines, COS-7 (African green monkey kidney cell line transformed with SV40) and the human osteosarcoma cell line U2OS. Imaging, RNAseq and lipidomic data reveal new findings that couple peroxisomal homeostasis to cholesterol trafficking, retinoic acid signaling, ribosome biogenesis and the integrated stress response.

## Results

### Depletion of peroxisomal LONP2 caused peroxisomal dysfunction in COS-7 cells and U2OS cells

To induce acute peroxisome-specific damage, we silenced LONP2 over 6 days in COS-7 and U2OS cells. Immunoblotting of LONP2-silenced cells after 6 days revealed an accumulation of the auto-cleaved products of the protease TYSND1, products established as LONP2 substrates [31], indicating that the efficiency of proteolytic processing of LONP2 inside peroxisomes was impaired (Fig. 1a and c). While there was an accumulation of these autocleaved forms of TYSND1, the remaining enzyme appeared functional since a known TYSND1 substrate, ACOX1, was processed normally (Additional file 1: Fig. S1). The precursor form of ACOX1 was reduced, perhaps reflecting a reduction in import. Analysis of peroxisomal membrane protein PMP70, the luminal protein thiolase (ACAA1) or catalase did not reveal a reduction in either of the protein levels, indicating that the peroxisomal mass was generally unchanged (Fig. 1a and c, Additional file 1: Fig. S3). Confocal microscopy demonstrated that peroxisomes were less abundant, but individual peroxisomes were elongated and enlarged in both cell lines (Fig. 1b and d).

The mechanisms of peroxisomal luminal and membrane protein import are distinct [9]. To monitor the import efficiency of luminal proteins, we transiently transfected cells with a peroxisome lumen-targeting sequence serine-lysine-leucine (SKL) fused with the Cyan Fluorescent Protein (CFP) and labelled peroxisomes with peroxisomal membrane protein PMP70. CFP-SKL was efficiently targeted to peroxisomes in control cells, but no longer imported into peroxisomes in LONP2-silenced COS-7 cells (Fig. 1e and f) or U2OS cells (Additional file 1: Fig. S2), demonstrating that the knockdown of LONP2 impaired peroxisomal luminal protein import. To evaluate the efficiency of peroxisomal membrane protein import, we used adenoviral expression of peroxisomal biogenesis factor 3 (PEX3) tagged with Yellow Fluorescent Protein (PEX3-YFP), whose import was unaltered in LONP2-silenced COS-7 cells (Fig. 1g). These data establish that depletion of LONP2 in both cell lines leads to alterations

in proteolysis of substrates like TYSND1 and inhibits protein import of our reporter CFP-SKL into the peroxisomal lumen without affecting membrane protein insertion. Given that the expression levels of endogenous peroxisomal proteins seen by western blot were mostly unchanged, including the processing of TYSND1 substrates like ACOX1, it suggests that the overall effect of LONP2 silencing on peroxisomal protein content is relatively mild after 6 days of silencing.

Loss of mitochondrial LONP1 leads to the accumulation of aggregated matrix content and the eventual initiation of autophagy-mediated organellar turnover, or mitophagy [58]. Thus, we evaluated whether LONP2 leads to the induction of pexophagy by monitoring levels and localization of LC3, a marker of autophagic membranes, and autophagic cargo adapter p62. As a positive control, we induced non-selective autophagy, using HBSS media, starving the cells of essential amino acids [42]. This resulted in an increased number of LC3-p62 puncta on peroxisomes (Fig. 1i, left). However, the number of peroxisomes colocalized with transiently expressed GFP-LC3 and the endogenous p62 was unchanged between non-targeted (*NT*-) and *LONP2*-silenced cells after 6 days (Fig. 1i, right). Moreover, LONP2 knockdown did not induce global autophagy, as LC3 isoforms and p62 remained unchanged in COS-7 cells (Fig. 1h). These data are consistent with the analysis of peroxisome morphology, which shows enlarged organelles, and immunoblots that showed no change in peroxisomal proteins like PMP70 and thiolase (Fig. 1a-d).

Peroxisomal import failure can lead to the targeting of peroxisomal proteins to mitochondria with detrimental consequences on mitochondrial function, metabolism, and cristae architecture [30]. Specifically, the abrogation

of *Pex3* or *Pex19*, core components of peroxisomal membrane insertion, resulted in the mitochondrial import of a series of peroxisomal membrane, and some luminal, proteins [30]. In addition, alterations in peroxisomal handling of generated as a by-product of mitochondrial respiration reactive oxygen species (ROS) by catalase or peroxiredoxins, or aberrant beta-oxidation of very long chain fatty acids can induce mitochondrial dysfunction [15]. Although *Pex3*-YFP was correctly targeted to peroxisomes in cells lacking LONP2 (Fig. 1g), we further examined whether LONP2 knockdown altered mitochondrial morphology by using Mitochondrial Network Analysis (MiNa), a semi-automated ImageJ plugin [48]. Confocal imaging of mitochondria stained with MitoTracker Deep Red FM demonstrated that mitochondrial network morphology remained unchanged upon silencing of LONP2 (Fig. 1j). Next, we employed the fluorescent dye MitoSOX that specifically detects ROS, and electrochemical potential-dependent TMRE stain. Confocal microscopy showed unaltered TMRE stain, but enhanced accumulation of MitoSOX-stained superoxide within mitochondria in *LONP2*-silenced COS-7 cells (Additional file 1: Fig. S4a). Surprisingly, MitoSOX-stained superoxide did not accumulate within mitochondria in *LONP2*-silenced U2OS cells (Additional file 1: Fig. S4b). Since peroxisomal phenotypes upon silencing LONP2 were consistent between the two cell lines, mitochondrial superoxide accumulation in COS-7 cells likely arises from impaired mitochondrial redox status, rather than is caused directly by peroxisomal proteotoxic stress.

Taken together, the loss of LONP2 alters peroxisomal morphology and numbers without initiation of pexophagy or altering mitochondrial network morphology, and in COS-7 cells results in accumulation of mitochondrial ROS.

(See figure on next page.)

**Fig. 1** LONP2 knockdown triggered the accumulation of its substrate TYSND1, alterations in peroxisome size and numbers, and luminal protein import failure. **a-d** Immunoblotting (**a, c**) and representative confocal images and quantification of peroxisome size and numbers (**b, d**) in non-targeting (*NT*-) and *LONP2*-silenced COS-7 cells (**a, b**) and U2OS cells (**c, d**) after 144 h. TYSND1-F and TYSND1-C indicate full-length TYSND1 and the self-cleaved C-terminal region of TYSND1, respectively. Scale bar, 5  $\mu$ m. **e, f** Representative confocal images (**e**) and quantification (**f**) of the colocalization between peroxisomes (PMP70) and transiently expressed peroxisome luminal protein (CFP-SKL) in *NT*- and *LONP2*-silenced COS-7 cells after 144 h. Scale bar, 2  $\mu$ m. **g** Representative confocal images showing the colocalization between peroxisomes (PMP70) and transiently expressed peroxisome membrane protein (PEX3-YFP) in *NT*- and *LONP2*-silenced COS-7 cells after 144 h. Scale bar, 5  $\mu$ m. **h** Immunoblotting for autophagy-related proteins, vinculin was used as a loading control. **i** Representative confocal images of COS-7 cells grown in HBSS for 24 h (left) and quantification (right) showing the number of LC3-P62 puncta on peroxisomes of *NT*- and *LONP2*-silenced COS-7 cells and U2OS cells after 144 h. Cells were grown in either DMEM or HBSS for 24 h and LC3-P62 puncta on peroxisome was visualized with transiently expressed GFP-LC3 and the immunofluorescence of p62 and PMP70. Scale bar, 2  $\mu$ m. **j** Representative confocal images and quantification showing the size and mean branch length of mitochondria in *NT*- and *LONP2*-silenced COS-7 cells after 144 h. Scale bar, 5  $\mu$ m. On all plots, dots represent individual cells from  $n=3$  technically independent experiments depicted in different colours, and triangles represent the mean within an independent experiment. The mean values were used to calculate the average (horizontal bar), s.d. (error bars), and *P*-values (using a two-tailed unpaired Student's *t*-test)

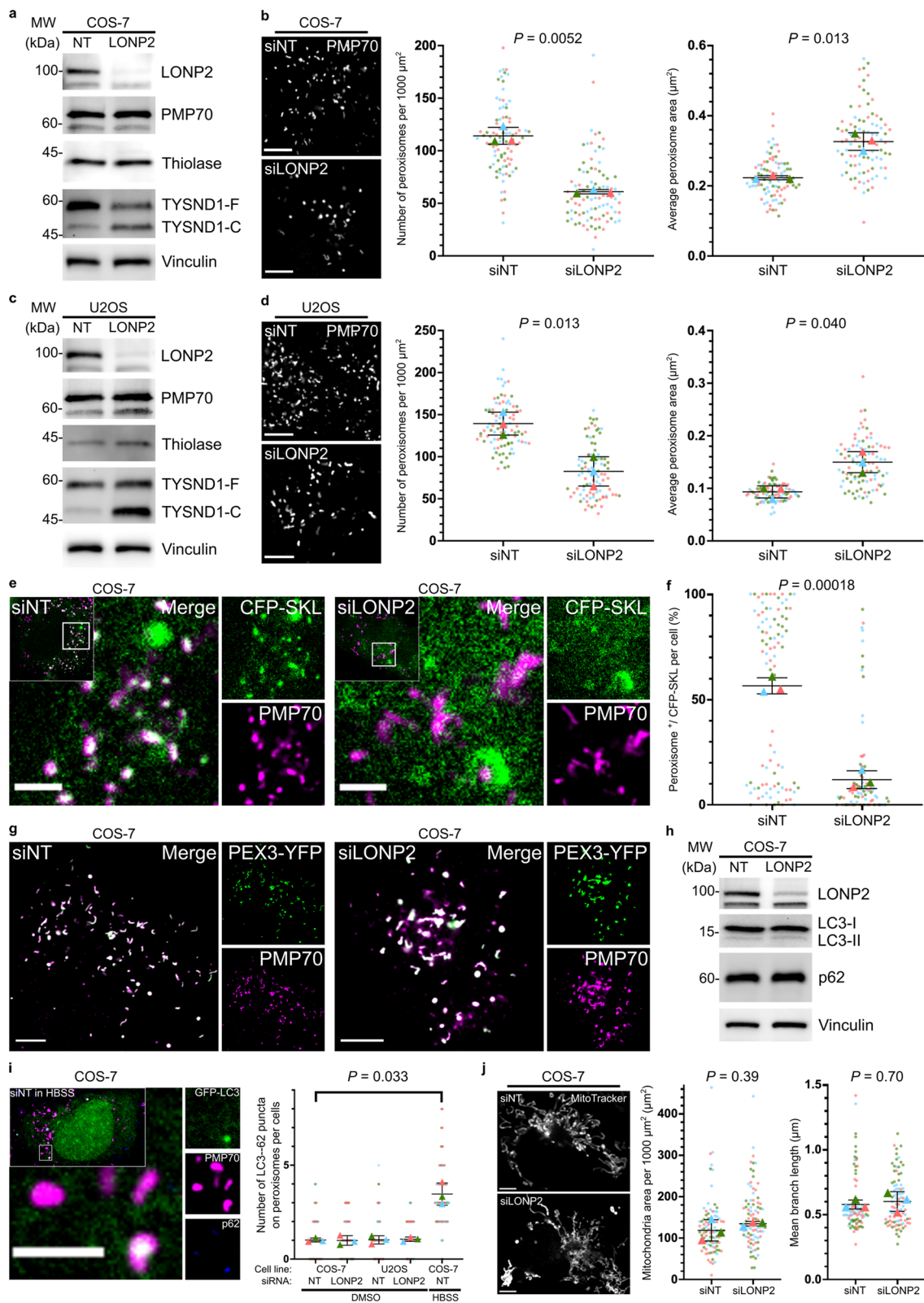


**Fig. 1** (See legend on previous page.)

### Peroxisomal proteotoxic stress leads to ISR and ribosome biogenesis activation in a cell specific manner

The specificity of mitochondrial ROS accumulation to COS-7 cells hinted that the loss of LONP2 may lead to global stress responses, which however may be uncoupled from the primary peroxisomal phenotypes common in both cell lines. To investigate the overall cell responses to LONP2 silencing, we analyzed transcriptomes of NT- and LONP2-silenced cells using RNA sequencing (RNAseq) in COS-7 and U2OS cells. Surprisingly, the gene expression response resulting from the loss of LONP2 between the two lines was drastically different (Fig. 2a and b, Additional file 2: Table S1), despite similar peroxisomal morphology and import phenotypes, and the relatively mild effects on overall peroxisomal protein content (Fig. 1c--g). Unsupervised principal component analysis showed that NT- and LONP2-silenced samples separated clearly in COS-7 but not U2OS line (Fig. 2a). In COS-7, expression levels of 3835 genes were downregulated and 3215 genes were upregulated ( $|\log_2(\text{FC})| > 0.5$ ,  $p_{\text{adj}} < 0.05$ ), while in U2OS expression levels of only 182 and 77 genes were down- and up-regulated, respectively ( $|\log_2(\text{FC})| > 0.5$ ,  $p\text{-value} < 0.01$ ) (Fig. 2b, Additional file 2: Table S1, and see Methods for details on thresholding of statistical significance).

As we anticipated a stress response signature upon loss of LONP2, we focused our analysis on the integrated stress response (ISR). The ISR is an evolutionary conserved eukaryotic signaling pathway that acts to attenuate cap-dependent translation via phosphorylation of eukaryotic translation initiation factor (eIF2), while simultaneously inducing one or more ISR effectors [activating transcription factors (ATF) ATF3, 4, 5, C/EBP homologous protein (CHOP) encoded by *DDIT3*] and their downstream targets [6, 32]. ISR effectors ATF3-5, CHOP, and several of their targets were induced in LONP2-depleted COS-7 but not U2OS cells (Fig. 2c and d). Consistent with this signature, we observed a dramatic reduction of protein synthesis (a key consequence of eIF2a phosphorylation during the ISR) in COS-7 but not U2OS cells, detected by puromycin labelling for 10 min [43] (Fig. 2e). Induction of global cellular stress in LONP-2 depleted COS-7 cells was further evidenced by the activation of apoptosis-associated cleaved caspases 3

and 7, increased DNA damage (as monitored by  $\gamma$ 2HAX phosphorylation) and induction of a regulator of innate immunity transcription factor NF- $\kappa$ B (Fig. 2d). These effects were not observed upon LONP2 depletion in U2OS cells. Together, these data suggest that proteotoxic peroxisomal stress activates ISR in a cell-type-specific manner. This is also consistent with the increased Mito-SOX staining in COS-7 but not U2OS cells (Additional file 1: Fig. S4b).

We also observed a global upregulation of mRNAs encoding factors implicated in ribosome biogenesis in LONP2-depleted COS-7, but not U2OS cells (Fig. 2f). Expression of a core mediator of ribosomal assembly RRS1 was also increased at the protein level (Fig. 2g) [16]. This was unexpected, since ribosome biogenesis is generally suppressed under stress [23, 29, 46], and LONP2-depletion in COS-7 cells resulted in strong reduction in protein synthesis (Fig. 2e). Collectively, these findings suggest that in addition to induction of ISR, depletion of peroxisomal LONP2 results in altered ribosome biogenesis in COS-7 cells.

A core goal of stress responses to organellar dysfunction is to restore homeostasis, which often includes upregulation of chaperone proteins, and in this case, potentially peroxisomal proteins. A previous report in *C.elegans* characterizing the response to PEX5 deletion noted the upregulation of peroxisomal genes driven by the activation of transcription factors PPAR $\alpha$ /MED15 orthologues [37]. However, in both COS-7 and U2OS, depletion of LONP2 did not result in an upregulation of peroxins or peroxisomal genes (Additional file 1: Fig. S5).

### Peroxisomal proteotoxic stress leads to defective retinoic acid signalling

While the ISR was not induced in U2OS cells, we sought to identify common responses to peroxisomal proteotoxic stress between COS-7 and U2OS cells, given that they both exhibited altered peroxisomal morphology and reduced import of the reporter CFP-SKL. Gene ontology analysis of transcripts changed in both cell lines revealed a significant downregulation of the retinoic acid (RA) / vitamin A signalling pathway

(See figure on next page.)

**Fig. 2** Cell-specific ISR activation upon silencing of LONP2. RNA sequencing ( $n = 3$  independent experiments per condition), LONP2 silencing for 7 days. **a** Principal component (PC) score plot. **b** Volcano plots showing all identified transcripts. **c** Transcripts encoding integrated stress response (ISR) factors. **d** Immunoblotting for ISR-related proteins, vinculin was used as a loading control. **e** Translation assay: cells were incubated with puromycin for 10 min., and incorporation of puromycin into newly synthesized proteins was revealed with anti-puromycin antibodies. GAPDH was used as a loading control. **f** Transcripts encoding ribosomal biogenesis-related rRNA, snoRNA and mRNA genes. **g** Immunoblot of ribosomal biogenesis regulator RRS1 in NT- and LONP2-silenced COS-7 cells and U2OS cells

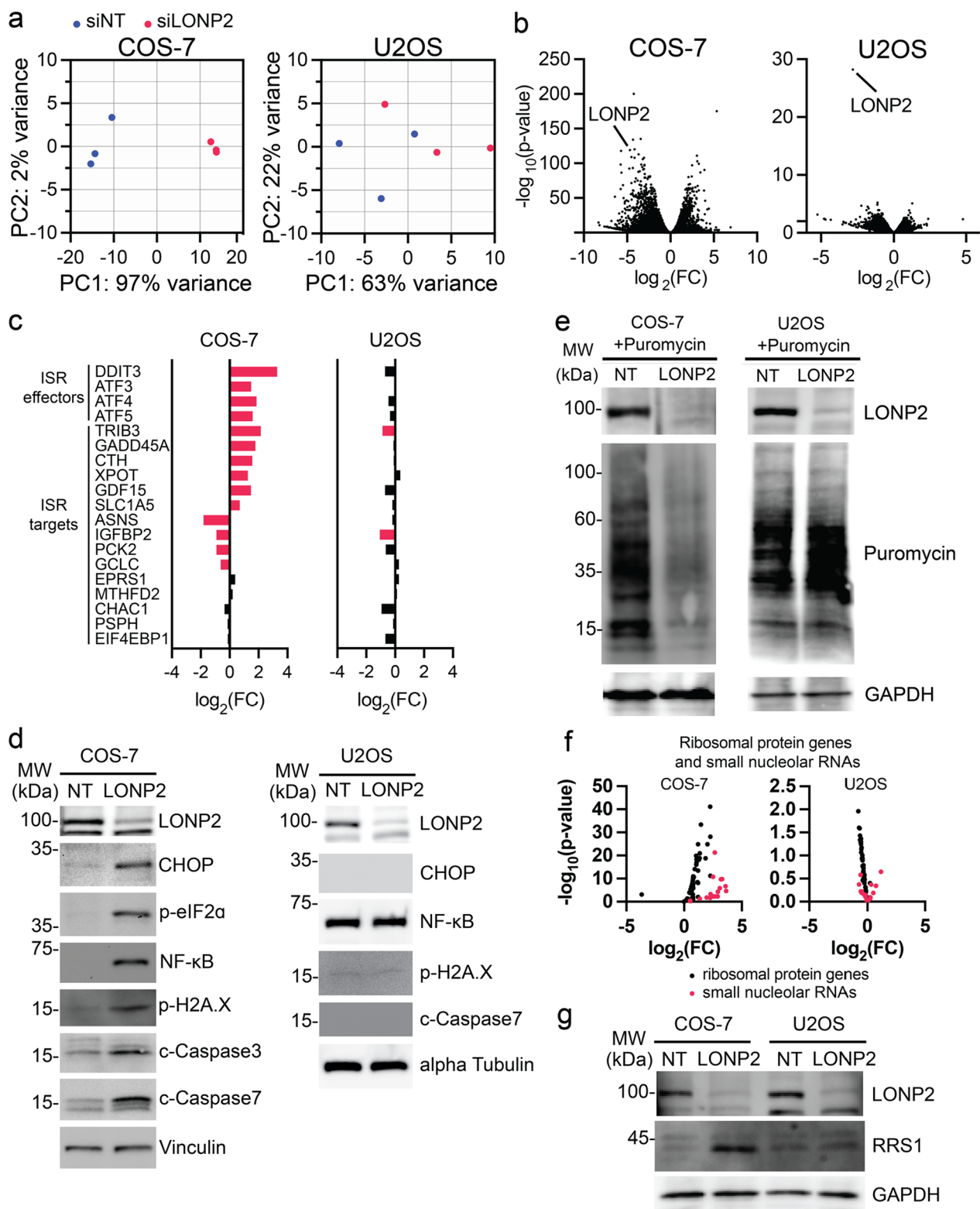


**Fig. 2** (See legend on previous page.)

[33] as a top hit (Fig. 3a). We validated this at the protein level by immunoblotting key proteins involved in RA signaling pathway: cellular all-trans retinoic acid (ATRA) binding proteins (CRABP2) and aldehyde dehydrogenase 1 family member A2 (ALDH1A2) [35] (Fig. 3b). Consistent with the RNAseq data, CRABP2 levels were strongly reduced in both COS-7 and U2OS. However, a second enzyme on this pathway, ALDH1A2, was not changed in U2OS, suggesting that the effects at the protein level in this cell line may be partial.

To test the functional consequence of the downregulation of RA signaling enzymes, we treated cells with all-*trans* retinoic acid (ATRA) to activate RA signaling and drive transcription of specific gene targets. RT-qPCR analysis confirmed the efficiency of LONP2 silencing in both cell lines (Fig. 3c). Upon ATRA treatment, the transcriptional upregulation of a retinoic acid-responsive gene, *Transglutaminase 2* (*TGM2*), was strongly suppressed in LONP2 knockdown in COS-7 cells, but only mildly altered in U2OS (Fig. 3c). Indeed, levels of *TGM2* mRNA were reduced in COS-7 cells treated with siLONP2 even prior to ATRA stimulation. Collectively, these data uncover the impact of peroxisomal dysfunction on retinoic acid signaling pathways.

#### Lipidomic analysis revealed accumulation of sphingomyelins and cholesterol esters in LONP2 silenced cells

One of the core functions of peroxisomes is in the generation and catabolism of specific lipids. Therefore, to investigate the effect of LONP2 knockdown on the regulation of lipid homeostasis, we performed comprehensive untargeted lipidomics in both COS-7 and U2OS cells. The dataset retained 2,094 mass spectrometry features, defined by their *m/z*, retention time and signal intensity. Similar to gene expression data, the lipidomic changes resulting from the loss of LONP2 between the two lines were drastically different as can be seen from the score plot of unsupervised principal component analysis (Fig. 4a). Among the 2,094 features of the final dataset, 467 (22%) of them passed our selected threshold ( $|\log_2(\text{FC})| > 1.5$ ,  $P_{\text{corr}}\text{-value} < 0.05$ ) as significantly different between the two cell lines under basal condition (Additional file 1: Fig. S6a, Additional file 3: Table S2), whereas upon depletion of LONP2 (vs. siNT), 242 were changed in COS-7 and 234 in U2OS cells (Additional file 1: Fig. S6b). It is notable that the lipid profile differed more markedly between the two cell lines at baseline (~22% were significantly different) than upon silencing of LONP2 within each cell line (~11% significantly different). These differences in lipidome profiles may suggest

that the specific flux or wiring of lipid synthesis and turnover pathways may underlie the sensitivity of COS-7 cells to mild alterations in peroxisomal proteostasis upon silencing LONP2.

Given the untargeted nature of lipidomic analysis, only lipid features of interest have been annotated, which for this study are those that passed the selected threshold of significance for the impact of LONP2 silencing in COS-7 and U2OS cell lines (See Methods for details). A total of 206 lipid features were annotated using MS/MS and data alignment with our in-house database [10] and were found to belong to different lipid subclasses (Fig. 4b). The most significantly changed unique lipid species upon LONP2 silencing in COS-7 cells and U2OS cells, which were annotated using MS/MS (22 and 25 unique lipids, respectively), are shown as box plots (Fig. 4c).

From these data, we conclude that for all three group comparisons conducted in this study, glycerophospholipids, specifically phosphatidylcholines (PC), showed the highest number of significantly up- or downregulated lipid features (red dots; Fig. 4b), reflecting substantial remodeling of their fatty acyl side chains. Under the basal state, sphingolipids, both sphingomyelins and glucosylceramides, as well as cholesterol esters were more abundant in COS-7 cells compared to U2OS cells (SP and ST; Fig. 4b). Upon LONP2 silencing, COS-7 and U2OS cells shared some lipid changes: namely downregulation of PCs (Fig. 4b and orange boxes in Fig. 4c), upregulation of sphingolipids, namely sphingomyelins (SM) such as SM(d34:0) and glucosylceramides (SP in Fig. 4b; Purple boxes in Fig. 4c; Fig. S6c) and of lipids containing a saturated or monounsaturated very long chain fatty acyl side chain (VLCFA  $\geq 22$  carbon chains in bold, Fig. 4c).

There were, however, important differences between these two cell lines in the response to LONP2 silencing for other lipid subclasses. For example, and of relevance to cholesterol metabolism, cholesterol ester (CE) CE20:1 or CE22:1 showed a striking  $\sim 4 \log_2(\text{FC})$  accumulation in LONP2-silenced COS-7 cells ( $P_{\text{corr}} = 0.000091$ ). The accumulation of these CEs in LONP2-silenced U2OS cells was less prominent, and variable (upregulated in 2 samples, unchanged in 3), therefore did not pass our significance threshold ( $\log_2(\text{FC}) = 1.36$ ,  $P_{\text{corr}} = 0.26$ ) (Fig. 4b and c, Additional file 1: Fig. S6c, Additional file 3: Table S2). A prominent set of ceramide species were also upregulated in COS-7 cells, many of which carried acyl chains  $\geq 22$  carbons. In contrast, ether PC was upregulated in LONP2-silenced U2OS but not COS-7 cells (Brown boxes in Fig. 4c).

Given the striking accumulation of CEs in LONP2-silenced COS-7 cells vs. LONP2-silenced U2OS cells, we further investigated the sensing of the excess cholesterol in our system. For this, we analyzed the expression of the

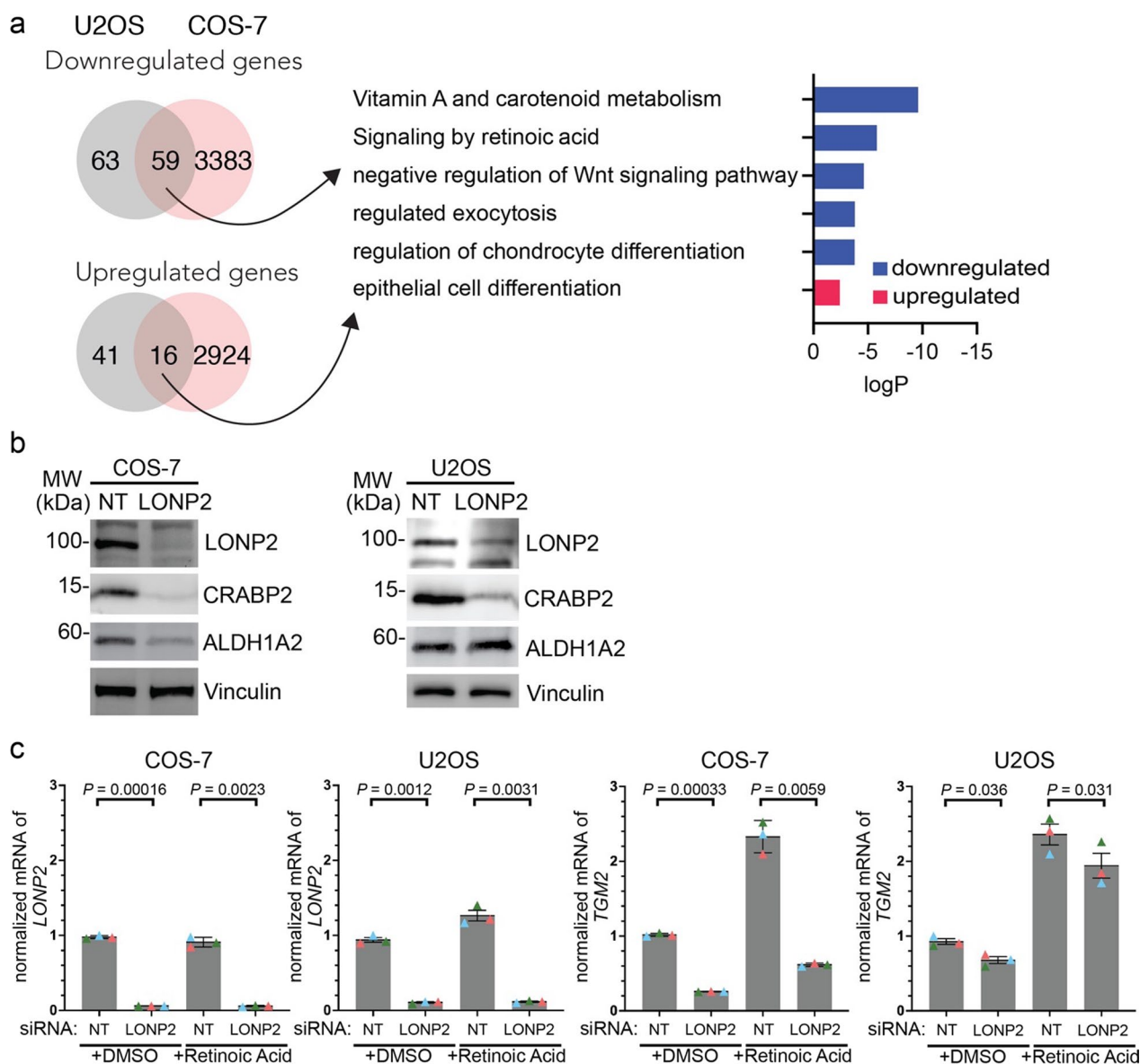


**Fig. 3** LONP2 silencing leads to impaired retinoic acid signaling. **a** Gene ontology of RNA sequencing data (dataset is described in Fig. 2). Numbers on Venn diagram indicate the number of genes in each category. **b** Immunoblotting of retinoic acid regulating proteins, vinculin used as a loading control. **c** COS-7 or U2OS cells were incubated in the presence or absence of 5  $\mu$ M retinoic acid for 24 h and mRNA transcript levels for LONP2 (left two panels) and TGM2 (right two panels) quantified with qRT-PCR.  $n = 3$  independent experiments, means are depicted in different colours. The mean values were used to calculate the average (horizontal bar), s.d. (error bars) and  $P$ -values (using a two-tailed unpaired Student's  $t$ -test)

ER membrane protein insulin-induced gene 1 (INSIG1), a core sensor within the cholesterol biosynthetic pathway that is rapidly degraded in response to the cholesterol depletion [4, 38]. Surprisingly, INSIG1 showed downregulation with immunoblotting (Fig. 4d) and RNAseq ( $\log_2(\text{FC}) = 3.34$ ,  $p.\text{adj} = 2.56\text{E-}14$ ) in COS-7 cells. In U2OS, INSIG1 mRNA and protein remained unchanged (Fig. 4d, RNAseq  $\log_2(\text{FC}) = 0.17$ ,  $p.\text{value} = 0.44$ ). Thus, concurring with lipidomic data, these results show that

in COS-7 cells, cholesterol is accumulated upon peroxisomal proteotoxic stress, but the loss of INSIG1 suggests that ER cholesterol sensing is impaired.

#### Cholesterol flux analysis shows accumulation in endolysosomes in response to LONP2 depletion

Impaired sensing of excess cholesterol in LONP2 depleted cells prompted us to examine the subcellular localization of the elevated cholesterol. For this,

we stained cholesterol with Filipin. Confocal imaging showed cholesterol staining to be abundant in both Nile Red-stained lipid droplets, and endolysosomes marked with lysosomal-associated membrane protein 1 (LAMP1) (Fig. 5a-b). LONP2 knockdown also led to an increased number of lipid droplets (Fig. 5a), consistent with increased triglycerides seen in lipidomics analysis (TG in Fig. 4b).

To monitor the flux of cholesterol in the absence of LONP2, we incubated cells with excess free cholesterol for one hour and stained them with Filipin. As with the endogenous cholesterol, confocal microscopy showed enhanced accumulation of Filipin within endolysosomes in both *LONP2*-silenced COS-7 and U2OS cells as compared to corresponding controls (Fig. 5c and d, left). Filipin staining was observed in less than 8% of endolysosomes in control COS-7 or U2OS cells, which rose to approximately 30% of endolysosomes in *LONP2*-silenced COS-7 and U2OS cells (Fig. 5c and d, right). The accumulation of cholesterol in lysosomes is reminiscent of the phenotypes in human lysosomal storage diseases, such as Niemann-Pick disease type C (NPC) caused by pathogenic variants in *NPC1* or *NPC2*, which block cholesterol export from the lysosome [34]. Indeed, electron microscopic analysis of *LONP2*-silenced COS-7 cells revealed many lamellated structures and electron-dense particles that strongly resembled the abnormal lysosomes observed in NPC cells (Fig. 5e). This included the presence of lipid whorls and lamellar inclusions, consistent with the observation that LONP2 depletion impaired sphingomyelin and cholesterol homeostasis (Fig. 5e).

Our results indicate that LONP2 knockdown impairs the ability of cholesterol to efflux from endolysosomes. Trapping of cholesterol in endolysosomes may lead to cholesterol depletion within the ER, driving INSIG1 degradation (Fig. 4d). This was specific to COS-7 cells, which started with significantly higher levels of sphingomyelins, glucocylceramides and cholesterol esters relative

to U2OS cells. This may indicate that the steady-state flux of cholesterol and sphingomyelins are much higher in COS-7 at steady state, rendering them more sensitive to LONP2 depletion. Indeed, only upon addition of excess cholesterol for flux analysis in U2OS cells did we observe similar phenotypes to COS-7 cells with the accumulation of cholesterol in endolysosomes. This is consistent with previous work suggesting that peroxisomes are required for the flux of cholesterol from the late endosome to the ER [5]. To investigate whether the lower steady-state cholesterol flux renders U2OS cells resistant to overall cellular responses to peroxisomal proteotoxic stress, we incubated U2OS cells with excess free cholesterol and assessed the impact of cholesterol overloading on the ISR activation at different time courses (2 h, 6 h and 24 h). Although confocal microscopy showed the lysosomal accumulation of Filipin-stained cholesterol at every time course upon silencing of LONP2 (Additional file 1: Fig. S7), LONP2-depletion did not induce the activation of CHOP in cholesterol loaded U2OS cells (Additional file 1: Fig. S8), suggesting that additional factors are required to activate the ISR. Taken together, our data establish a critical requirement for functional peroxisomes in the trafficking of cholesterol and lipid droplet biogenesis.

To exclude the possibility of off-target effects in our LONP2 silencing experiments, COS-7 cells were transfected with different siRNA targeting the 3' UTR of *LONP2* and then rescued by transient expression of si-resistant *LONP2* cDNA. Immunoblotting revealed that CHOP activation, as well as downregulation of INSIG1 and CRABP2 were fully rescued by the transient expression of *LONP2* cDNA (Fig. 5f, left). Cholesterol homeostasis was also rescued functionally, as free cholesterol no longer accumulated at endolysosomes after transfection of *LONP2* cDNA for 48 h (Fig. 5f, right).

(See figure on next page.)

**Fig. 4** Lipid profiles of COS-7 and U2OS cells differ drastically and are differentially affected by LONP2 silencing. Untargeted lipidomic analysis of  $n=5$  independent cell experiments for each group under the basal condition of after *LONP2*-silencing for which the final dataset included 2,094 lipid features (Table S2). **a** Principal component (PC) score plot. **b** Log<sub>2</sub> (fold changes) of 206 lipid features annotated by MS/MS and data alignment using our in-house database, and grouped by lipid subclass, whereby red and black dots indicate lipids that reach or not our selected significance threshold for the indicated comparison,  $P_{corr}$ -value < 0.1. **c** Box plots of unique lipids annotated by MS/MS from the 100 most significant lipid features discriminating *LONP2*-silenced COS-7 cells (top) and U2OS cells (bottom) from *NT*-silenced cells. The midline represents the median fold change vs. *NT*-silenced cells, the box represents the interquartile range between the first and third quartile, and the whiskers represent the lowest or highest values. **d** Immunoblotting of cholesterol sensor INSIG1, vinculin used as a loading control. Abbreviations: sphingolipid (SP), sterol lipid (ST), glycerolipid (GL), glycerophospholipid (GP), fatty acyls (FA), sphingomyelin (SM), ceramide (Cer), glucosylceramide (GlcCer), cholesterol (Chol), cholesterol ester (CE), triacylglycerol (TG), diacylglycerol (DG), 1-alkyl, 2-acylglycerophosphocholine (PCO-), 1-(1Z-alkenyl), 2-acylglycerophosphocholine (PCP-), 1-alkyl, 2-acylglycerophosphoethanolamine (PEO-), 1-(1Z-alkenyl), 2-acylglycerophosphoethanolamine (PEP-), diacylglycerophosphocholine (PC), diacylglycerophosphoethanolamine (PE), diacylglycerophosphoinositol (PI), monoacylglycerophosphocholine (LPC), monoacylglycerophosphoethanolamine (LPE), diacylglycerophosphoglycerol (PG), free fatty acid (FFA) and acylcarnitine (CAR). All lipid features were categorized into subclasses and labeled based on the LIPID MAPS® Structure Database

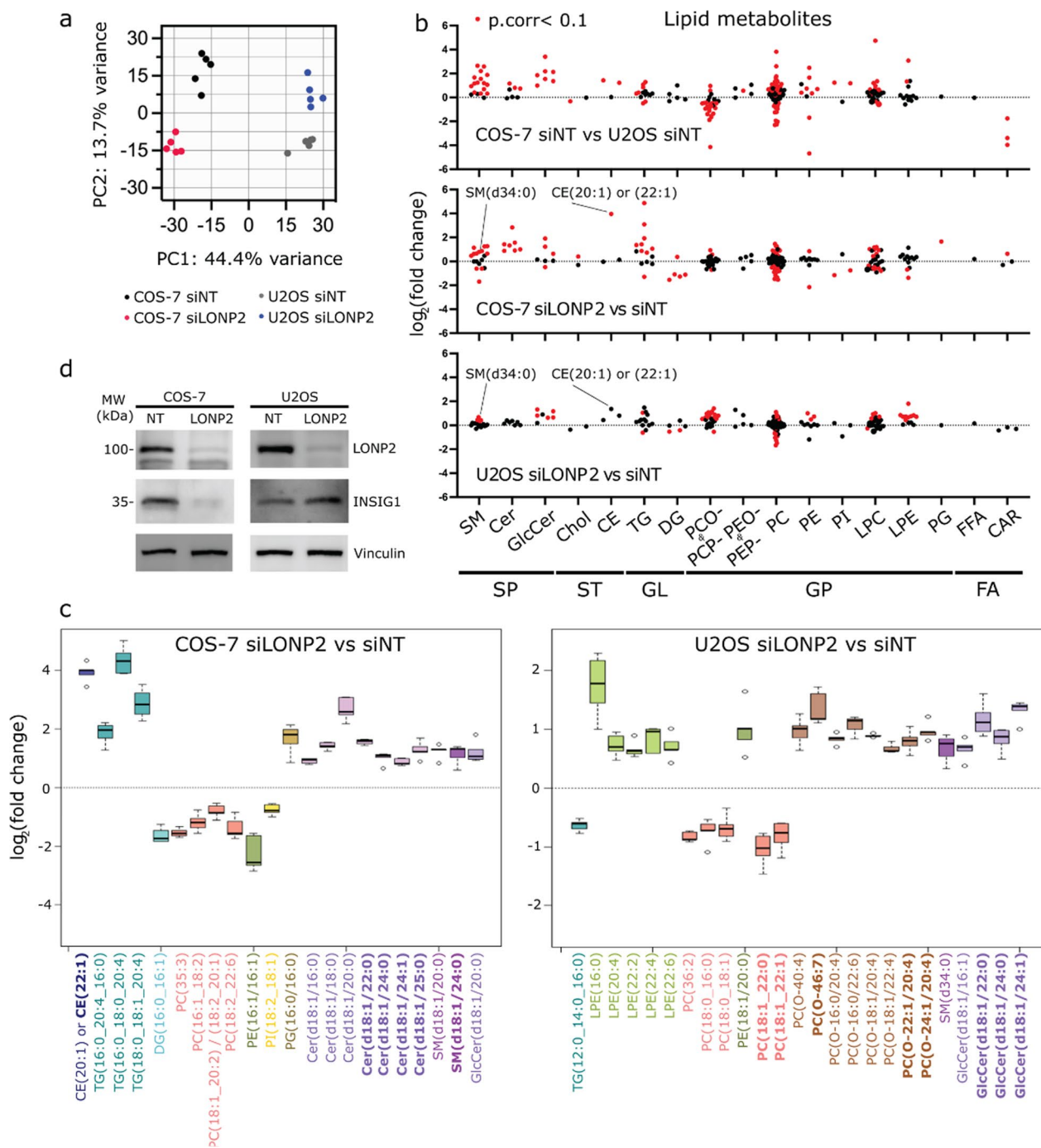


**Fig. 4** (See legend on previous page.)

**Specificity of response to siLONP2 relative to loss of Pex5**  
 Previous approaches to investigate peroxisomal stress pathways focused on loss of core peroxins essential for protein import in *C. elegans*, *Drosophila* and mammalian cells [25, 30, 37, 53]. LONP2 is a chaperone and protease that is important for the turnover and proteostasis within peroxisomes, and, as we demonstrated here,

is required for the import of at least some luminal proteins. Therefore, we tested whether the pathways that are induced by LONP2 silencing are also triggered by the loss of core import proteins like PEX5 in our system. As with the loss of LONP2, PEX5-depleted COS-7, but not U2OS cells displayed clear upregulation of ISR effector CHOP, as well as downregulation of the ER cholesterol

sensor INSIG1 (Additional file 1: Fig. S9). In contrast to the depletion of LONP2 however, PEX5 silencing failed to bolster expression of the ribosomal assembly protein RRS1 or retinoic acid CRABP2 protein levels (Additional file 1: Fig. S9). These intriguing differences suggest that luminal peroxisomal proteotoxic stress induces distinct responses relative to global peroxisomal protein import failure.

## Discussion

Data presented here extend and identify new consequences of peroxisomal dysfunction, including induction of the ISR, disruption of cholesterol regulation and trafficking, and altered retinoic acid signalling. Our data highlight the significant variability in the dependence of different cell types on peroxisomal function. Importantly, our strategy to manipulate the peroxisomal protease/chaperone LONP2 allowed us to maintain peroxisomal membrane protein import and thus avoid the direct induction of mitochondrial stress through the mitochondrial import of peroxisomal proteins [30].

Our data showed that loss of LONP2 led to changes in peroxisome morphology, where cells had fewer and larger organelles, suggesting that LONP2 function was directly or indirectly required for peroxisomal division. While we expected to observe the induction of pexophagy as part of a peroxisomal quality control response, we saw no induction of autophagy or changes in peroxisomal mass. This suggests that the consequence of LONP2 silencing on peroxisomal protein composition was relatively mild. For example, while we observed an accumulation of LONP2 substrate TYSND1, the functional impact of this was not yet seen on TYSND1 substrate ACOX1. In addition, while the acute transfection of CFP-SKL demonstrated a failure to import in LONP2 silenced cells, the import defects were not sufficient to reduce expression of the endogenous peroxisomal proteins we examined with the exception of the precursor of ACOX1. Our approach allowed us to capture the early stages of peroxisomal dysfunction sufficient to explore both common consequences of LONP2 loss and the dramatic cell-specific

induction of the ISR. We did not observe a transcriptional induction of peroxisomal biogenesis (including PPAR genes), a repair mechanism seen in previous investigations into the peroxisome stress response pathways (Additional file 2: Table S1)[37].

Lipidomics, RNAseq and cell biological analysis presented here further establish peroxisomes as a critical contributor to cholesterol homeostasis and intracellular flux. This is consistent with recently published evidence that peroxisomes form direct contact sites with lysosomes to flux cholesterol to the ER [5]. To this end, syntrophin7 (*syt7*) was identified as the essential tether between peroxisomes and lysosomes to drive cholesterol flux. We observed no apparent changes in *syt7* mRNA levels (Additional file 2: Table S1). We thus suspect that the loss/aggregation of an unidentified peroxisomal luminal protein interfered with this pathway of cholesterol flux. The loss of INSIG1 was also seen upon loss of PEX5 in COS-7 cells, indicating that impaired cholesterol trafficking may occur upon diverse peroxisomal dysfunctions. Untargeted lipidomics also revealed an increase in mono- or un-saturated very long chain fatty acyl chains among the significantly changed lipids, suggesting peroxisomal dysfunction in beta-oxidation pathways upon depletion of LONP2. Interestingly, these changes were enriched within ceramide and sphingomyelin species in COS-7, but within ether lipids and glucosylceramides in U2OS. This is further indication that peroxisomes play important, yet differential roles in the wiring of lipid metabolism between the two cell lines. The impact of these elevated lipids on cell survival may be reflected in the increased caspase activation in COS-7, where ceramides are tightly linked to an enhanced apoptosis [28]. The increased ether lipids may alter the susceptibility of U2OS cells to ferroptotic death pathways, as highlighted in recent studies linking peroxisomal function to the ferroptosis [57]. Future work will continue to explore the contribution of peroxisomal lipid metabolism to cell survival pathways.

Another common pathway altered upon loss of LONP2 (but not PEX5) in both cell lines was a prominent

(See figure on next page.)

**Fig. 5** LONP2 knockdown induced lipid storage, including aberrant cholesterol accumulation in lysosomes. **a** Representative confocal images (left) and quantification (right) of lipid droplets (Nile Red) in *NT*- and *LONP2*-silenced COS-7 cells after 6 days. Scale bar, 5  $\mu$ m. **b** Representative confocal images showing the Filipin-stained intracellular cholesterol (green), Nile Red-stained lipid droplets (magenta) and endolysosomes (blue) visualized with the immunofluorescence of LAMP1. Scale bar, 2  $\mu$ m. **c, d** Free cholesterol overload experiment in *NT*- and *LONP2*-silenced COS-7 cells (**c**) and U2OS cells (**d**) after 7 days. Representative confocal images (left) and quantifications (right) of the colocalization between cholesterol (Filipin) and endolysosomes (LAMP1). Scale bar, 2  $\mu$ m. **e** Transmission electron microscopy micrographs of *NT*- and *LONP2*-silenced COS-7 cells. Scale bar, 500 nm. **f** Immunoblotting (left) and image quantification (right) of cholesterol overload experiment in *NT*- and *LONP2*-silenced COS-7 cells rescued with transient expression of siRNA-resistant LONP2 cDNA for 48 h. Data from  $n = 3$  technically independent experiments, and their respective means are depicted in different colours. The mean values were used to calculate the average (horizontal bar), s.d. (error bars) and *P*-values (using a two-tailed unpaired Student's *t*-test)

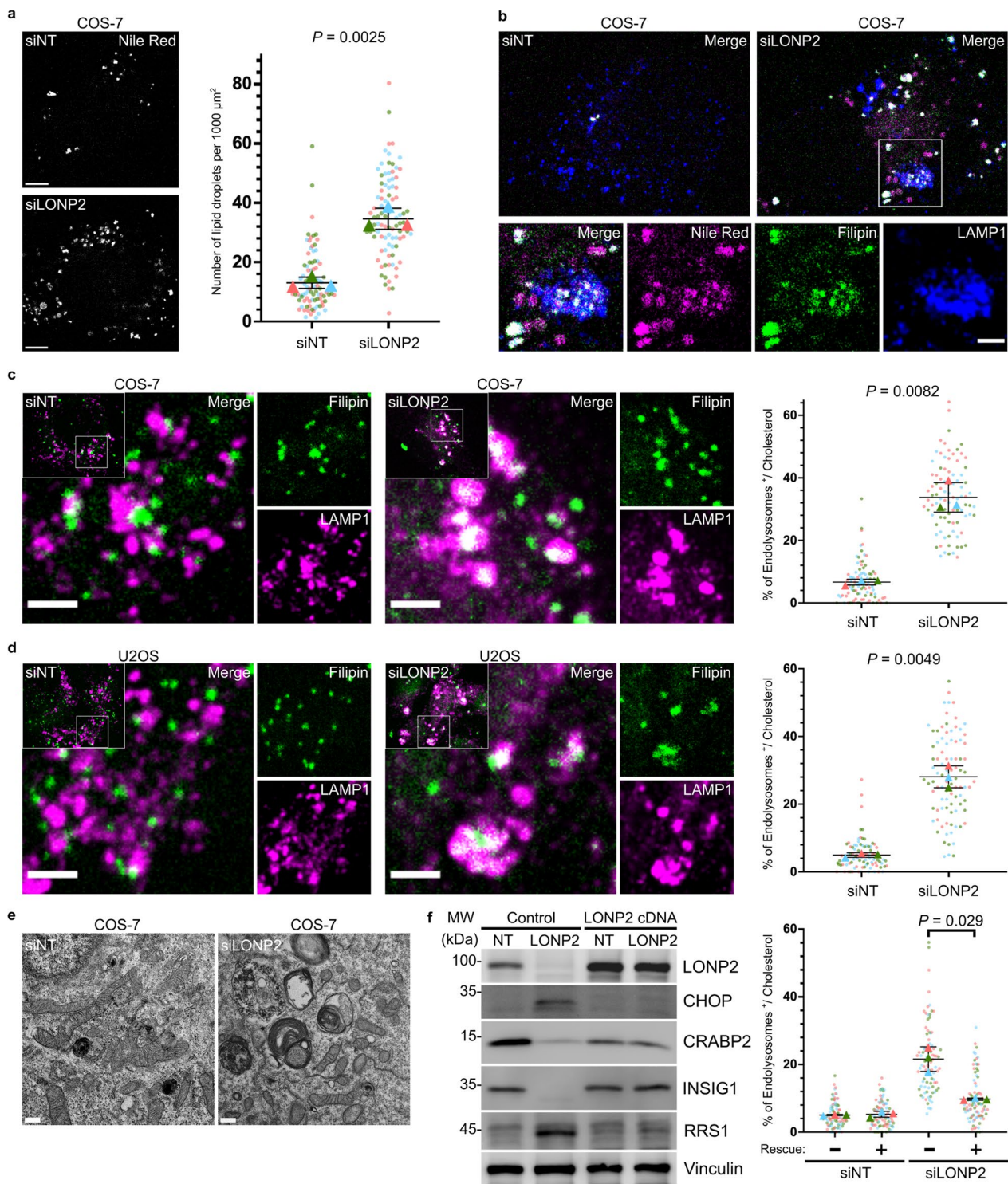


**Fig. 5** (See legend on previous page.)

downregulation of the retinoic acid/Vitamin A pathway. Retinoic acid is a branched chain lipid that plays a key role in a plethora of both essential in development, and disease-related pathways [35]. Historically, retinoic acid

has been described as a peroxisome proliferator [14] and a possible link between peroxisomes and lipid droplets [39]. Intriguingly, RA signaling pathway has been linked to peroxisomal function in the liver, specifically to bile

acid and cholesterol metabolism [41]. Retinoic acid binds to the nuclear receptor RXR, which controls gene expression of a host of genes and can form dimers with up to 10 other nuclear hormone receptors including regulators of bile acid metabolism and lipid homeostasis [33]. Of relevance to peroxisomes, knockout of RXR $\alpha$  in mouse hepatocytes leads to a sevenfold upregulation of a key regulator of bile acid metabolism CYP7A1, again linking retinoic acid signaling and peroxisomal function [51]. Our data suggest a retrograde signaling pathway from peroxisomes into the RXR signaling pathway as well. Future work will explore the physiological, tissue specific regulation to unravel how and why the loss of LONP2 results in the downregulation RA signaling.

Additional responses to LONP2 depletion included the COS-7-specific induction of the ISR, and the increased mRNA transcripts linked to ribosome biogenesis. The ISR is a highly conserved stress response pathway, classical triggers of which include amino acid or heme deprivation, viral infection, and ER stress [32]. ISR is seen as a pro-survival mechanism, however recent studies demonstrated the context-specific and time-sensitive role of the response in a variety of pathologies including models of neurodegenerative and mitochondrial diseases [6, 20, 44]. Our study establishes peroxisomal proteotoxic stress as a new ISR trigger, providing a potential target for therapeutic interventions. COS-7 cells lacking LONP2 also demonstrated increased transcription of ribosome biogenesis messages that included rRNA, snoRNA and mRNAs. Interestingly, PEX5 loss did not lead to the increased expression of RRS1, a core regulator of ribosomal biogenesis, yet showed a clear activation of the ISR with CHOP expression. Another recent study showed significant downregulation of mRNA linked to ribosome biogenesis upon loss of peroxins [17], a trend also seen in our Pex5 depletion experiment. Therefore, the ribosome biogenesis response can be uncoupled from the peroxisome-driven activation of the ISR and appears to be specific to the loss of LONP2.

The acute silencing approach allowed us to observe the immediate response to the loss of a core peroxisomal chaperone/protease, avoiding the confounding effects of cellular adaptation in complete loss of function models. Our data suggest that the cell-specific responses reflect a differential dependence on peroxisomal functions in lipid handling between cell types and tissues. Peroxisomes exhibit profound functional plasticity depending on the tissue context, driving bile acid synthesis in the liver to the generation of ether lipids in oligodendrocytes, and scavenging ROS [52]. It will be important to further explore the consequences of peroxisomal stress in tissues and disease states, where the study of dynamic lipid handling and flux may be studied in more physiological

settings. Understanding the contributions of peroxisomes to cholesterol flux in liver during bile acid synthesis, or within development/cancer model systems where peroxisomes may impact retinoic acid metabolism, could open doors to new therapeutic targets in multiple disease settings from Zellwegers syndrome to metabolic disorders and cancer.

## Materials and methods

### Culturing of cell lines

COS-7 (ATCC, CRL-1651) and U2OS (ATCC, HTB-96) cells were cultured in Dulbecco's modified Eagle medium (DMEM) containing 4.5 g l<sup>-1</sup> glucose, GLUTA-PLUS and sodium pyruvate (Wisent, 319-027-CL) supplemented with 100  $\mu$ M non-essential amino acids (Gibco, 11,140,050) and 10% fetal bovine serum (Wisent, 085-150). All cells were cultured at 37 °C and 5% CO<sub>2</sub> in a humidified incubator and regularly tested for mycoplasma using the MycoAlert mycoplasma detection kit (Lonza, LT07-418).

### Transfection and RNA interference of cells

For transient transfection, 1  $\mu$ g plasmid DNA per well was transfected into cells for 16 h at a confluency of 60% in 6-well plates using Lipofectamine 3000 (Invitrogen, L3000001) according to the manufacturer's recommendations. The following plasmids were used: CFP-SKL [27], GFP-LC3 [19] and pCMV3-hLONP2 (SinoBiological, HG25229-UT). The siRNA-mediated knockdown of proteins was performed for 144 h or 168 h using Lipofectamine RNAiMAX (Invitrogen, 13,778,150) diluted in Opti-MEM (Invitrogen, 31,985-070) and checked by immunoblotting. Briefly, cells with a confluency of 30–40% were transfected with specific siRNAs or a non-targeting control according to the manufacturer's instructions. After 72 h transfection, the cells were collected, reseeded into 6-well plates, and transfected with the same siRNAs or a non-targeting control for another 72 h or 96 h transfection. The following human siRNAs were used: LONP2 (Dharmacon, ON-TARGETplus, J-005933-06-0005), LONP2 (Dharmacon, Accell, A-005933-14-0005), PEX5 (Dharmacon, ON-TARGETplus, J-015788-07) and non-targeting control (D-001810-10).

### Adenovirus infection

C-terminal YFP-fused PEX3 was subcloned into D2-MCS viral vector (BioVector) under the control of a CMV promoter as described previously [45]. Adenoviral PEX3-YFP was used to infect cells at 100 pfu per cell in the presence of 4  $\mu$ g/ml polybrene (Sigma, H9268-10G) for 16 h.

### Immunofluorescence microscopy

Cells were seeded into 24-well plates on glass coverslips and fixed in 5% PFA in PBS, at 37 °C for 15 min, then washed three times with PBS, followed by quenching with 50 mM ammonium chloride in PBS. After three washes in PBS, cells were permeabilized in 0.1% Triton X-100 in PBS, followed by three washes in PBS. The cells were blocked with 10% FBS in PBS, followed by incubation in 5% FBS in PBS for 16 h at 4 °C with primary antibodies (1:1,000) to the following: ACOX1 (Proteintech, 10,957-1-AP), Catalase (millipore, 219,010), LAMP1 (Cell Signaling, 9091), p62 (Cell Signaling, 8025) and PMP70 (Sigma, SAB4200181). After three washes with 5% FBS in PBS, cells were incubated in 5% FBS in PBS for 1 h at RT with appropriate secondary antibodies (1:2,000): cross-adsorbed goat anti-rabbit IgG (H+L) Alexa 594 (Invitrogen, A11012), anti-mouse IgG (H+L) Alexa 647 (Invitrogen, A21235) and anti-rabbit IgG (H+L) Alexa 647 (Invitrogen, A21244). For cholesterol or lipid droplet staining, cells were incubated with 50 µg/ml Filipin (Sigma, SAE0087) for an hour or with 1 µg/ml Nile Red (Sigma, 72,485) for 10 min, respectively. After five washes in 5% FBS in PBS, coverslips were mounted onto slides using fluorescence mounting medium (Dako). Cells were imaged using a 100× objective NA1.4 on an IX83 inverted microscope (Olympus) with appropriate lasers using a spinning disc system microscope (Yokogawa) coupled to a Neo camera (Andor). For quantification analysis, 30 cells in each condition were randomly chosen and counted based on the definitions on main figures (number and size of peroxisomes: Fig. 1b and 1d; percentage of peroxisomes colocalized with CFP-SKL: Fig. 1f and Additional file 1: Fig. S1; the number of LC3-p62 puncta on peroxisomes: Fig. 1i; mitochondrial network analysis: Fig. 1j; the number of lipid droplets: Fig. 5a; percentage of endolysosomes colocalized with cholesterol: Fig. 5c, d, and f).

### Live cell imaging

Cells plated in a glass-bottom cell culture dish (MatTek) were incubated with 250 nM TMRE (Sigma) and 1 µM MitoSOX™ Green (Invitrogen) for 30 min at 37 °C. Cells were washed in DMEM and observed in DMEM containing no phenol red (GIBCO) supplied with 10% FBS and 2 mM L-glutamine, NEAA and 10 mM HEPES pH 7.4 using a spinning disk confocal microscope (described above) with a 100× objective and EMCCD camera. For quantification analysis, 30 cells in each condition were randomly chosen and examined if the MitoSOX signal was colocalized with mitochondria to calculate percentage of cells with MitoSOX-positive mitochondria.

### Cell lysates and immunoblotting

To obtain whole cell lysates for western blot analysis, cells were harvested by centrifugation at 15,000 g for 10 min and solubilized with HEPES lysis buffer (1% (wt/vol) Triton X-100, 1 mM EDTA, 50 mM HEPES pH7.4, and 150 mM NaCl). The total protein concentration was determined by using a Bradford assay (Bio-Rad) and the lysates were mixed with sample buffer (10% (vol/vol) glycerol, 2% (wt/vol) SDS, 0.005% (wt/vol) bromophenol blue, 60 mM Tris-HCl pH6.8 and 10% (vol/vol) β-mercaptoethanol) and heated at 95 °C for 5 min before loading, followed by SDS-PAGE using gradient gels with ranges of 4–16% acrylamide. Proteins were transferred to nitrocellulose membranes and primary antibodies (1:1,000) to the following proteins were used for the immunodetection of proteins using horseradish peroxidase-conjugated anti-mouse (Cytiva, NA931) and anti-rabbit (Cytiva, NA934) secondary antibodies (1:1,000): Catalase (millipore, 219,010), CHOP (Cell Signaling, 5554), Cleaved Caspase-3 (Cell Signaling, 9661), Cleaved Caspase-7 (Cell Signaling, 9491), CRABP2 (Proteintech, 10,225-1-AP), GAPDH (Abcam, AB9485), INSIG1 (Santa Cruz, sc-390504), LC3 (Novus Biological, NB100-2331), LONP1 (Proteintech, 15,440-1-AP), NF-κB (Cell Signaling, 6956), p62 (Cell Signaling, 8025), PEX5 (Cell Signaling, 83,020), Phospho-eIF2α (Sigma, SAB4504388), Phospho-γH2AX (Abcam, AB2893), PMP70 (Sigma, SAB4200181), Puromycin (Sigma, MABE343), RRS1 (Proteintech, 15,329-1-AP), Thiolase (Sigma, HPA007244), TYSND1 (Sigma, HPA030304), and Vinculin (Sigma, V4505).

### RNAseq analysis

Total RNA was extracted from each cell using RNeasy Plus (QIAGEN) after 168 h siRNA transfection, and the quantity and quality was determined using Bioanalyzer (Agilent Technologies). Single read sequencing was performed with NextSeq 500 (Illumina) using 75 cycles High Output kit v2. Sequences were trimmed for sequencing adapters and low quality 3' bases using Trimmomatic version 0.35 [3] and aligned to the reference *Chlorococcus sabaeus* genome version ChlSab1.1 (gene annotation from Ensembl 104) or *Homo sapiens* genome version GRCh38 (gene annotation from Gencode version 37) using STAR version 2.7.1a [7].

Raw gene expression counts were obtained directly from STAR, and normalization and differential expression analysis were performed using DESeq2 version 1.30.1 [24]. Metascape software was used for gene ontology analysis [56]. We used unadjusted *p*-values for U2OS analysis as false discovery rate calculation has low power

in datasets with small effect sizes (i.e. low fraction of changed genes in RNAseq) [22], and in our dataset Benjamini–Hochberg procedure resulted in over-represented  $p$ -adjusted values (Additional file 2: Table S1). For comparison analyses between COS-7 and U2OS, gene identifiers were converted from *C. sabaeus* to *H. sapiens* using the R/Bioconductor package biomaRt (version 2.48.3).

#### RT-qPCR

Total RNA was isolated from each cell using RNeasy kit (QIAGEN) after 168 h siRNA transfection. RT–qPCR and data analysis were performed at IRIC Genomics Platform (University of Montreal). All reactions were run in triplicate and the average values of Ct were used for quantification. The relative quantification of target genes was determined using the  $\Delta\Delta$ CT method. Primers for target genes are as follows: LONP2 (COS-7) (Fw: gtgggaagatcagtgccaa, Rv: gcctgtgtcctcgaatgca), LONP2 (U2OS) (Fw: ggggacgtgatgaaggagtc, Rv: agcattgtcagctgtact), TGM2 (Fw: cggatgctgtgtacctggac, Rv: cttgatgaactggccgagc), TBP (endogenous control) (Fw: gaacatcatggatcagaacaaca, Rv: atagggattccgggagtc) and YWHAZ (endogenous control) (Fw: gcaattactgagagacaacttgaca, Rv: tgggaaggccggttaatttt).

#### Puromycylation assay

Translation intensity was monitored by the incorporation of puromycin as previously described [43]. After 7 days siRNA transfection, cells were pulsed with 10  $\mu$ g/ml puromycin (Sigma, P8833) at 37 °C for 10 min. Cells were then harvested as described above and blots probed with anti-puromycin antibodies, as described above.

#### Retinoic acid stimulation

COS-7 cells were incubated in the presence or absence of 5  $\mu$ M retinoic acid (Sigma, R2625) at 37 °C for 24 h before isolating total RNA for analysis by qRT-PCR.

#### Untargeted lipidomics

Lipid extraction, sample and data analysis were performed using a previously validated semi-quantitative untargeted lipidomic workflow [10]. In brief, lipids were extracted from each cell after 168 h siRNA transfection and spiked with six internal standards: LPC 13:0, PC19:0/19:0, PC14:0/14:0, PS12:0/12:0, PG15:0/15:0, and PE17:0/17:0 (Avanti Polar Lipids). Protein concentration was determined using a colorimetric-based assay based on the Bradford dye-binding method and samples were injected into a 1290 Infinity high-resolution HPLC coupled with a 6530 Accurate Mass quadrupole

time-of-flight (LC-QTOF) (Agilent Technologies) via a dual electrospray ionization (ESI) source. Elution of lipids was assessed on a Zorbax Eclipse plus column (Agilent Technologies) maintained at 40 °C using an 83 min chromatographic gradient of solvent A (0.2% formic acid and 10 mM ammonium formate in water) and B (0.2% formic acid and 5 mM ammonium formate in methanol/acetonitrile/methyl tert-butyl ether [MTBE], 55:35:10 [v/v/v]). Data acquisition was performed in positive ionisation mode. All samples were processed and analyzed as a single batch. MS quality controls (QCs) were performed by (i) injecting 3 “in-house” QC samples and blanks at the beginning, middle and end of the run and (ii) monitoring six internal standards spiked in samples for signal intensity, mass mass-to-charge ratios ( $m/z$ ) and retention time (RT) accuracies. Mass spectrometry (MS) raw data processing was achieved as previously described using Mass Hunter B.06.00 (Agilent Technologies) for peak picking and an in-house bioinformatic script [2018, Forest et al.] in both Perl and R languages that we developed for: (i) MS feature peak alignment and retention time (RT) correction; (ii) filter of presence: features retained must be present in 80% of samples from at least one group, thereby setting a maximum of 20 missing values within a group; (iii) normalization of signal intensities using cyclic loess algorithm; (iv) imputation of missing values to 90% of lower values. The resulting final dataset included 2,094 high-quality MS signals, thereafter referred to as features, defined by their  $m/z$ , RT and signal intensity (listed in Additional file 3: Table S2). Statistical analyses are performed using the final dataset on log<sub>2</sub>-transformed signal intensity data. An unsupervised principal component analysis was first applied followed by independent testing of each feature using or two-tailed unpaired Student's  $t$ -test with Benjamini–Hochberg correction for the indicated group comparison. Given the untargeted nature of our lipidomic analysis, only lipid features of interest have been annotated to unique lipids, a step that is crucial given that about 50% of all MS features are duplicate ions of the same lipid. For this study, lipid annotation was focused on the features that passed the selected threshold of significance, namely  $P_{corr}$ -value ( $P$  value after Benjamini–Hochberg multiple testing correction) of  $<0.05$  and an absolute fold change (FC)  $|FC| > 1.5$  (corresponding to  $|\log_2(FC)| > 0.58$ ) for the comparisons siLONP2 vs. siNT in COS-7 and U2OS. Lipid annotation was achieved as previously described in details (Forest et al.) by (i) MS/MS analysis for the 100 most significant lipid features in each comparison and (ii) through data alignment with our in-house database, which contains  $>500$  unique lipids with previously determined MS/MS spectra for the remaining significant features.

### Cholesterol flux analysis

Cholesterol was delivered to cells by a cholesterol-cyclodextrin complex (Sigma, C4951) that contained approximately 40 mg of cholesterol per gram of material. All treatment concentrations were calculated based on cholesterol weight. After 168 h siRNA transfection, cells were incubated with 200  $\mu$ M cholesterol in a culture medium at 37 °C for an hour, washed and incubated in a culture medium for an hour, followed by fixation and immunofluorescence microscopy. For the cholesterol overloading experiment (Additional file 1: Fig. S6 and S7), U2OS cells were fixed at different time courses after the addition of 200  $\mu$ M cholesterol (2 h, 6 h and 24 h).

### Transmission electron microscopy

Electron microscopy (EM) was performed as previously described [27]. After 168 h siRNA transfection, cells were fixed with 5% PFA and 1.6% glutaraldehyde (GA) in 0.1 M sodium cacodylate buffer (pH 7.4) for 10 min at RT, then further fixed at 4 °C in the same buffer overnight. After washing with 0.1 M cacodylate buffer, cells were fixed with 1% osmium tetroxide for 60 min at 4 °C, washed with water, stained with saturated aqueous uranyl acetate for 45 min at RT, and then gradually dehydrated with a series of increasing concentrations of ethanol (70–100%). After dehydrating with 100% acetone, cells were gradually embedded in Spurr's resin, and polymerized for 48 h at 60 °C. Samples were sectioned to a 100-nm thickness and sections were mounted on 200-mesh copper grids, and sections were imaged at 120 kV using a FEI Tecnai 12 TEM outfitted with an AMT XR80C CCD Camera System, housed in the Facility for Electron Microscopy Research (FEMR) at McGill University.

### Statistics and reproducibility

Statistical significance was tested by the unpaired two-tailed Student's *t*-test using the GraphPad Prism software (version 8.4.3). The values of all individual cells and the mean of each experiment are shown for the quantification analysis. Error bars displayed on graphs represent the means  $\pm$  SD of at least three independent technical replicates. Graphs were generated using Prism or R.

### Supplementary Information

The online version contains supplementary material available at <https://doi.org/10.1186/s13062-023-00416-3>.

**Additional file 1.** Supplementary figures.

**Additional file 2.** The file contains the following sheets, preceded with 'U2OS' or 'COS-7': 1. counts\_allgenes = raw read counts for all detected genes. 2. counts\_analysedgenes = raw not normalised read counts for genes with at least 4 reads in at least 3 samples in the dataset. This gene list was used for differential expression analysis. 3. Deseq2 = differential

expression analysis. 4. transformed reads\_vsd or transformed reads\_rlog = Deseq2 transformation of reads, used for generating heatmaps. 5. counts\_normalised = Deseq2 normalisation of reads, used for generating scatter and others plots of individual gene expression levels. 6. overlay sheets = overlay of COS-7 and U2OS datasets.

**Additional file 3.** This file contains 3 sheets. The first sheet "corrected abundance" presents the AUC (Area Under the Curve) values of the corrected signals for all present compounds in the analyzed samples, obtained following our "data processing" (For more details, see Forest et al. *J. Proteome Res.* 2018, 17, 3657-3670). The second sheet is "statistical analysis". The third sheet "statistics + abundance" present in one glance the data from the first 2 sheets that are combined.

### Acknowledgements

We are grateful for support from Sigrid Juselius Fellowship (OI), FRQS Studentship (AY) and a CRC (HMM). This work was funded by CIHR PJT-162183 (to HMM). We would like to thank members of the laboratory for critical reading of the manuscript.

### Author contributions

AY designed and performed experiments, contributed to manuscript preparation. OI contributed to analysis and presentation of both RNAseq and lipidomics datasets, helped design validation experiments, and contributed to the preparation of the manuscript. MN performed experiments and assisted AY in this work. RL performed RNAseq experiments, and KW provided analysis of RNAseq dataset. CD, IRF and CDR performed lipidomics experiments, analyzed and interpreted the data. IT provided expertise for puromycin experiments and expert advice related to ISR, ribosome assembly and translation. HMM designed and analyzed experiments, contributed to manuscript and figure preparation. All members of the team contributed to manuscript preparation and editing.

### Funding

We are grateful for support from Sigrid Juselius Fellowship (O.I.), FRQS Doctoral Fellowship (A.Y.) and a CRC (H.M.M.). This work was funded by CIHR PJT-162183 (to H.M.M.). Canadian Institutes of Health Research, PJT-162183

### Availability of data and materials

Table S1 shows all RNA sequencing data. Table S2 shows all lipidomics data. The raw data of RNA sequencing is available in NCBI GEO repository (accession no. GSE224992).

### Declarations

#### Ethics approval and consent to participate

Not applicable.

#### Competing interests

The authors declare no competing interests.

#### Author details

<sup>1</sup>Montreal Neurological Institute, McGill University, Montréal, QC, Canada. <sup>2</sup>Department of Anatomy and Cell Biology, McGill University, Montréal, QC, Canada. <sup>3</sup>Institute for Research in Immunology and Cancer, Université de Montréal, Montréal, Canada. <sup>4</sup>Department of Oncology-Pathology, Karolinska Institute, Stockholm, Sweden. <sup>5</sup>Montreal Heart Institute, Université de Montréal, Montréal, Canada. <sup>6</sup>Lady Davis Institute, McGill University, Montreal, Canada. <sup>7</sup>Gerald Bronfman Department of Oncology, McGill University, Montréal, QC, Canada. <sup>8</sup>Department of Biochemistry, McGill University, Montréal, QC, Canada. <sup>9</sup>Division of Experimental Medicine, McGill University, Montréal, QC, Canada.

Received: 27 March 2023 Accepted: 13 September 2023  
Published online: 22 September 2023

## References

- EB Aksam A Koek JA Kiel S Jourdan M Veenhuis IJ Klei van der 2007 A peroxisomal Lon protease and peroxisome degradation by autophagy play key roles in vitality of *Hansenula polymorpha* cells *Autophagy* 3 96–105
- M Bartoszewska C Williams A Kikhney L Opalinski CW Roermund van R Boer de M Veenhuis IJ Klei van der 2012 Peroxisomal proteostasis involves a Lon family protein that functions as protease and chaperone *J Biol Chem* 287 27380–27395
- AM Bolger M Lohse B Usadel 2014 Trimmomatic: a flexible trimmer for Illumina sequence data *Bioinformatics* 30 2114–2120
- MS Brown A Radhakrishnan JL Goldstein 2018 Retrospective on cholesterol homeostasis: the central role of scap *Annu Rev Biochem* 87 783–807
- BB Chu YC Liao W Qi C Xie X Du J Wang H Yang HH Miao BL Li BL Song 2015 Cholesterol transport through lysosome-peroxisome membrane contacts *Cell* 161 291–306
- Costa-Mattioli M, Walter P (2020) The integrated stress response: from mechanism to disease. *Science* 368:5314
- A Dobin CA Davis F Schlesinger J Drenkow C Zaleski S Jha P Batut M Chaisson TR Gingeras 2013 STAR: ultrafast universal RNA-seq aligner *Bioinformatics* 29 15–21
- A Eraso-Pichot M Braso-Vives A Golbano C Menacho E Claro E Galea R Masgrau 2018 GSEA of mouse and human mitochondriomes reveals fatty acid oxidation in astrocytes *Glia* 66 1724–1735
- Farre JC, Mahalingam SS, Proietto M, Subramani S. Peroxisome biogenesis, membrane contact sites, and quality control. *EMBO Rep.* 2019;20.
- Forest A, Ruiz M, Bouchard B, Boucher G, Gingras O, Daneault C, Robillard Frayne I, Rhainds D, iGenoMed C, Consortium NIG, Tardif JC, Rioux JD, Des Rosiers C. Comprehensive and reproducible untargeted lipidomic workflow using LC-QTOF validated for human plasma analysis. *J Proteome Res.* 2018;17:3657–3670
- L Gibellini A Gaetano De M Mandrioli E Tongeren Van CA Bortolotti A Cossarizza M Pinti 2020 The biology of Lonp1: more than a mitochondrial protease *Int Rev Cell Mol Biol* 354 1–61
- S Goto-Yamada S Mano C Nakamori M Kondo R Yamawaki A Kato M Nishimura 2014 Chaperone and protease functions of LON protease 2 modulate the peroxisomal transition and degradation with autophagy *Plant Cell Physiol* 55 482–496
- A He JM Dean IJ Lodhi 2021 Peroxisomes as cellular adaptors to metabolic and environmental stress *Trends Cell Biol* 31 656–670
- R Hertz J Bar-Tana 1992 Induction of peroxisomal beta-oxidation genes by retinoic acid in cultured rat hepatocytes *Biochem J* 281 Pt 1 41–43
- Hijazi I, Wang E, Orozco M, Pelton S, Chang A. Peroxisomal support of mitochondrial respiratory efficiency promotes ER stress survival. *J Cell Sci.* 2022;135.
- Y Hua J Song C Peng R Wang Z Ma J Zhang Z Zhang N Li L Hou 2021 Advances in the relationship between regulator of ribosome synthesis 1 (RRS1) and diseases *Front Cell Dev Biol* 9 620925
- Huang K, Kim J, Vo P, Miao T, Bai H. Peroxisome import stress impairs ribosome biogenesis and induces integrative stress response through eIF2 $\alpha$  phosphorylation. *bioRxiv.* 2021:2020-11.
- MS Ioannou J Jackson SH Sheu CL Chang AV Weigel H Liu HA Pasolli CS Xu S Pang D Matthies HF Hess J Lippincott-Schwartz Z Liu 2019 Neuron-astrocyte metabolic coupling protects against activity-induced fatty acid toxicity *Cell* 177 1522–1535 e1514
- Y Kabeya N Mizushima T Ueno A Yamamoto T Kirisako T Noda E Komiyama Y Ohsumi T Yoshimori 2000 LC3, a mammalian homologue of yeast Apg8p, is localized in autophagosomal membranes after processing *EMBO J* 19 5720–5728
- Kaspar S, Oertlin C, Szczepanowska K, Kukat A, Senft K, Lucas C, Brodesser S, Hatzoglu M, Larsson O, Topisirovic I, Trifunovic A. Adaptation to mitochondrial stress requires CHOP-directed tuning of ISR. *Sci Adv.* 2021;7.
- CM Kassmann C Lappe-Siefke M Baes B Brugger A Mildner HB Werner O Natt T Michaelis M Prinz J Frahm KA Nave 2007 Axonal loss and neuroinflammation caused by peroxisome-deficient oligodendrocytes *Nat Genet* 39 969–976
- M Krzywinski N Altman 2014 Points of significance: comparing samples-part I *Nat Methods* 11 215–216
- MS Lindstrom J Bartek A Maya-Mendoza 2022 p53 at the crossroad of DNA replication and ribosome biogenesis stress pathways *Cell Death Differ* 29 972–982
- MI Love W Huber S Anders 2014 Moderated estimation of fold change and dispersion for RNA-seq data with DESeq2 *Genome Biol* 15 550
- FD Mast J Li MK Virk SC Hughes AJ Simmonds RA Rachubinski 2011 A Drosophila model for the Zellweger spectrum of peroxisome biogenesis disorders *Dis Model Mech* 4 659–672
- ZA McGee CM Clemens RL Jensen JJ Klein LR Barley GL Gorby 1992 Local induction of tumor necrosis factor as a molecular mechanism of mucosal damage by gonococci *Microb Pathog* 12 333–341
- M Neuspiel AC Schauss E Braschi R Zunino P Rippstein RA Rachubinski MA Andrade-Navarro HM McBride 2008 Cargo-selected transport from the mitochondria to peroxisomes is mediated by vesicular carriers *Curr Biol* 18 102–108
- R Nganga N Oleinik B Ogretmen 2018 Mechanisms of ceramide-dependent cancer cell death *Adv Cancer Res* 140 1–25
- C Ni M Buszczak 2023 The homeostatic regulation of ribosome biogenesis *Semin Cell Dev Biol* 136 13–26
- E Nuebel JT Morgan S Fogarty JM Winter S Lettlova JA Berg YC Chen CU Kidwell JA Maschek KJ Clowers C Argyriou L Chen I Wittig JE Cox M Roh-Johnson N Braverman J Bonkowsky SP Gygi J Rutter 2021 The biochemical basis of mitochondrial dysfunction in Zellweger Spectrum Disorder *EMBO Rep* 22 e51991
- K Okumoto Y Kametani Y Fujiki 2011 Two proteases, trypsin domain-containing 1 (Tysnd1) and peroxisomal Lon protease (PsLon), cooperatively regulate fatty acid beta-oxidation in peroxisomal matrix *J Biol Chem* 286 44367–44379
- K Pakos-Zebrucka I Koryga K Mnich M Ljujic A Samali AM Gorman 2016 The integrated stress response *EMBO Rep* 17 1374–1395
- M Petkovich P Chambon 2022 Retinoic acid receptors at 35 years *J Mol Endocrinol* 69 T13–T24
- SR Pfeffer 2019 NPC intracellular cholesterol transporter 1 (NPC1)-mediated cholesterol export from lysosomes *J Biol Chem* 294 1706–1709
- E Pohl CWE Tomlinson 2020 Classical pathways of gene regulation by retinoids *Methods Enzymol* 637 151–173
- LC Pomatto R Raynes KJ Davies 2017 The peroxisomal Lon protease LonP2 in aging and disease: functions and comparisons with mitochondrial Lon protease LonP1 *Biol Rev Camb Philos Soc* 92 739–753
- E Rackles M Witting I Forne X Zhang J Zacherl S Schrott C Fischer JJ Ewbank C Osman A Imhof SG Rolland 2021 Reduced peroxisomal import triggers peroxisomal retrograde signaling *Cell Rep* 34 108653
- A Radhakrishnan JL Goldstein JG McDonald MS Brown 2008 Switch-like control of SREBP-2 transport triggered by small changes in ER cholesterol: a delicate balance *Cell Metab* 8 512–521
- WG Robison Jr T Kuwabara 1977 Vitamin A storage and peroxisomes in retinal pigment epithelium and liver *Invest Ophthalmol Vis Sci* 16 1110–1117
- GL Russo G Sonsalla P Natarajan CT Breunig G Bulli J Merl-Pham S Schmitt J Giehl-Schwab F Giesert M Jastroch H Zischka W Wurst SH Stricker SM Hauck G Masserdotti M Gotz 2021 CRISPR-mediated induction of neuron-enriched mitochondrial proteins boosts direct glia-to-neuron conversion *Cell Stem Cell* 28 524–534 e527
- A Saeed M Hoekstra MO Hoeke J Heegsma KN Faber 2017 The interrelationship between bile acid and vitamin A homeostasis *Biochim Biophys Acta Mol Cell Biol Lipids* 1862 496–512
- G Sargent T Zutphen van T Shatseva L Zhang V Giovanni Di R Bandsma PK Kim 2016 PEX2 is the E3 ubiquitin ligase required for pexophagy during starvation *J Cell Biol* 214 677–690
- EK Schmidt G Clavarino M Ceppi P Pierre 2009 SUNSET, a nonradioactive method to monitor protein synthesis *Nat Methods* 6 275–277
- EL Spaulding TJ Hines P Bais ALD Tadenev R Schneider D Jewett B Patavina SL Pratt KH Morelli MG Stum DP Hill C Gobet M Pipis MM Reilly MJ Jennings R Horvath Y Bai ME Shy B Alvarez-Castelao EM Schuman LP Bogdanik E Storkebaum RW Burgess 2021 The integrated stress response contributes to tRNA synthetase-associated peripheral neuropathy *Science* 373 1156–1161
- A Sugiura S Mattie J Prudent HM McBride 2017 Newly born peroxisomes are a hybrid of mitochondrial and ER-derived pre-peroxisomes *Nature* 542 251–254
- W Szafarski M Lesniczak-Staszak M Sowinski S Ojha A Aulas D Dave S Malla P Anderson P Ivanov SM Lyons 2022 Early rRNA processing is a stress-dependent regulatory event whose inhibition maintains nucleolar integrity *Nucleic Acids Res* 50 1033–1051

47. D Tsitsekian G Daras A Alatzas D Templalexis P Hatzopoulos S Rigas 2019 Comprehensive analysis of Lon proteases in plants highlights independent gene duplication events *J Exp Bot* 70 2185 2197
48. AJ Valente LA Maddalena EL Robb F Moradi JA Stuart 2017 A simple ImageJ macro tool for analyzing mitochondrial network morphology in mammalian cell culture *Acta Histochem* 119 315 326
49. FM Vaz S Ferdinandusse 2017 Bile acid analysis in human disorders of bile acid biosynthesis *Mol Aspects Med* 56 10 24
50. CL Walker LCD Pomatto DN Tripathi KJA Davies 2018 Redox regulation of homeostasis and proteostasis in peroxisomes *Physiol Rev* 98 89 115
51. YJ Wan D An Y Cai JJ Repa T Hung-Po Chen M Flores C Postic MA Magnuson J Chen KR Chien S French DJ Mangelsdorf HM Sucov 2000 Hepatocyte-specific mutation establishes retinoid X receptor alpha as a heterodimeric integrator of multiple physiological processes in the liver *Mol Cell Biol* 20 4436 4444
52. RJA Wanders M Baes D Ribeiro S Ferdinandusse HR Waterham 2023 The physiological functions of human peroxisomes *Physiol Rev* 103 957 1024
53. MF Wangler YH Chao V Bayat N Giagtzoglou AB Shinde N Putluri C Coarfa T Donti BH Graham JE Faust JA McNew A Moser M Sardiello M Baes HJ Bellen 2017 Peroxisomal biogenesis is genetically and biochemically linked to carbohydrate metabolism in *Drosophila* and mouse *PLoS Genet* 13 e1006825
54. A Wlodawer B Sekula A Gustchina TV Rotanova 2022 Structure and the Mode of Activity of Lon Proteases from Diverse Organisms *J Mol Biol* 434 167504
55. E Zalckvar M Schuldiner 2022 Beyond rare disorders: a new era for peroxisomal pathophysiology *Mol Cell* 82 2228 2235
56. Y Zhou B Zhou L Pache M Chang AH Khodabakhshi O Tanaseichuk C Benner SK Chanda 2019 Metascape provides a biologist-oriented resource for the analysis of systems-level datasets *Nat Commun* 10 1523
57. Y Zou WS Henry EL Ricq ET Graham VV Phadnis P Maretich S Paradkar N Boehnke AA Deik F Reinhardt JK Eaton B Ferguson W Wang J Fairman HR Keys V Dancik CB Clish PA Clemons PT Hammond LA Boyer RA Weinberg SL Schreiber 2020 Plasticity of ether lipids promotes ferroptosis susceptibility and evasion *Nature* 585 603 608
58. Zurita Rendon O, Shoubridge EA. LONP1 is required for maturation of a subset of mitochondrial proteins, and its loss elicits an integrated stress response. *Mol Cell Biol*. 2018;38.

## Publisher's Note

Springer Nature remains neutral with regard to jurisdictional claims in published maps and institutional affiliations.

Ready to submit your research? Choose BMC and benefit from:

- fast, convenient online submission
- thorough peer review by experienced researchers in your field
- rapid publication on acceptance
- support for research data, including large and complex data types
- gold Open Access which fosters wider collaboration and increased citations
- maximum visibility for your research: over 100M website views per year

At BMC, research is always in progress.

Learn more [biomedcentral.com/submissions](https://biomedcentral.com/submissions)

